Ferromagnetic Weyl fermions in CrO_2

R. Wang,[1,2] Y. J. Jin,[1] J. Z. Zhao,[1] Z. J. Chen,[1,3] Y. J. Zhao,[3] and H. Xu[1,*]

[1]*Department of Physics and Institute for Quantum Science and Engineering, Southern University of Science and Technology, Shenzhen 518055, People's Rebuplic of China*

[2]*Institute for Structure and Function and Department of Physics, Chongqing University, Chongqing 400044, People's Rebuplic of China*

[3]*Department of Physics, South China University of Technology, Guangzhou 510640, People's Rebuplic of China*

(Received 29 November 2017; revised manuscript received 3 May 2018; published 31 May 2018)

The interplay between symmetry and magnetization directions in ferromagnetic materials provides an exotic platform to investigate the symmetry-protected topological order. In this work, we propose that unexpected ferromagnetic topological features, such as triple fermions and type-I and type-II Weyl fermions, can emerge in three phases of chromium dioxide (CrO_2), i.e., rutile CrO_2, orthorhombic CrO_2 of the $CaCl_2$ type, and pyrite CrO_2. Using first-principles calculations and topology analysis, we reveal that the breaking of the spin-rotation symmetry leads to tunable Weyl fermions that are robust against spin-orbital coupling, which can be easily realized by manipulating the magnetization direction. In particular, rutile CrO_2, a well-known half-metallic ferromagnet used in magnetic recording tapes, is an ideal candidate to overcome obstacles of studying ferromagnetic topological semimetals in experiments. The topological features in different phases of CrO_2 may bridge the gap between the band topology and local chemical bonding. Our findings substantially advance the experimental realization of ferromagnetic Weyl semimetals. More importantly, room-temperature ferromagnetic Weyl fermions in CrO_2 may give rise to promising applications related to the topological phenomena in industry.

DOI: 10.1103/PhysRevB.97.195157

I. INTRODUCTION

Topological semimetals or metals, in which the conduction and valence bands cross each other near the Fermi level, resulting in topological protected nodal points or nodal lines in momentum space, are an emerging topological phase in a condensed-matter system. Accordingly, different fermions with nontrivial band topology have been proposed, i.e., fourfold-degenerate Dirac fermions [1,2], twofold-degenerate type-I or type-II Weyl fermions [3–7], three-degenerate triple fermions [8,9], node-line fermions [10], etc. These protected band degeneracies require a striking interplay of symmetry and topology in electronic structures of realistic materials. For instance, Dirac semimetal phases are protected by crystal rotational symmetry [1,2] or nonsymmorphic symmetry [11]; Weyl semimetal (WSM) phases require either broken spatial-inversion symmetry $\mathcal{I}$ [12] or broken time-reversal symmetry $\mathcal{T}$ [3,5]; node-line semimetals require a space-time inversion ($\mathcal{IT}$) with spin-rotation symmetry [13,14] or a mirror reflection [15,16]. Distinguished from normal semimetals or metals, the linear quasiparticle excitations in topological semimetals or metals lead to diverse exotic quantum features. In particular, WSMs which host the unique nodal points called Weyl points (WPs) with definite chirality, acting as a magnetic monopole in momentum space, exhibit interesting transport phenomena such as surface Fermi arcs, a chiral anomaly, and anomalous Hall effects [3–5,17,18]. Recently, WSMs were intensively studied theoretically [3,5,12,19–27] and were observed in the nonmagnetic TaAs family [28] and $MoTe_2$ [29].

In comparison with nonmagnetic topological semimetals, ferromagnetic (FM) topological semimetals with time-reversal symmetry breaking are promising materials for future spintronic devices due to their nontrivial electronic structures coexisting with intrinsic magnetic order [5,24,27,30]. As topological properties in FM topological semimetals closely depend on the magnetization direction, they will exhibit abundant topological quantum phenomena, providing an exotic platform to investigate the symmetry-protected topological order. Up to now, however, only a few FM topological semimetals have been proposed [5,24,27]. Topological fermions and accompanying nontrivial surface states in FM topological semimetals have not been successfully verified experimentally. It is well known that the observation of topological features in FM topological semimetals is challenging due to a number of experimental or theoretical obstacles, e.g., magnetic doping, magnetic domains, strong correlations, etc. [31]. Therefore, searching for reliable FM topological materials that will be easily verified in experiments is highly desired. Based on the discussions above, we suggest one attractive route to explore FM topological semimetals in widely used and well-known materials. This not only is in favor of experimental observations but also realizes room-temperature applications of FM topological semimetals.

In this work, we propose that three phases of CrO_2, i.e., rutile (r-)CrO_2, orthorhombic (o-)CrO_2 of the $CaCl_2$ type, and pyrite (p-)CrO_2, can possess type-I or type-II Weyl fermions that are strongly related to magnetic symmetries. The position and structure of WPs are tunable in different phases of CrO_2 by changing the magnetization direction with an externally applied magnetic field, providing a realistic and promising platform to study Weyl fermions with time-reversal symmetry

*xuh@sustc.edu.cn

breaking. In particular, r-CrO_2, a widely used magnetic recording material with a high Curie temperature in the range of 385–400 K [32,33], is an ideal candidate to study FM topological fermions in experiments. Importantly, we find that r-CrO_2, o-CrO_2, and p-CrO_2 share similar chemical bonds; that is, each Cr atom is surrounded by a distorted octahedron of six O atoms, implying that the topological features in different phases of CrO_2 highlight the link between the band topology and local chemical bonding [34].

II. COMPUTATIONAL METHODS AND CRYSTAL STRUCTURES

First-principles calculations are performed using the Vienna Ab initio Simulation Package (VASP) [35,36] based on the density functional theory (DFT) [37]. The core-valence electron interactions are treated using the projector augmented-wave [38] method. The exchange-correlation potential is chosen as the generalized gradient approximation with the Perdew-Burke-Ernzerhof formalism [39,40]. A plane-wave basis set with a kinetic-energy cutoff of 600 eV is used. The correlation effect of Cr $3d$ electrons is considered by introducing the effective on-site Coulomb energy $U = 3$ eV [41], which gives an appropriate description that is in excellent agreement with previously reported band structures and half-metallic properties of r-CrO_2 [42]. Importantly, FM topological features are robust with U over a wide range.

In ambient conditions, CrO_2 crystalizes in a rutile structure with space group $P4_2/mnm$ (No. 136), as shown in Fig. 1(a).

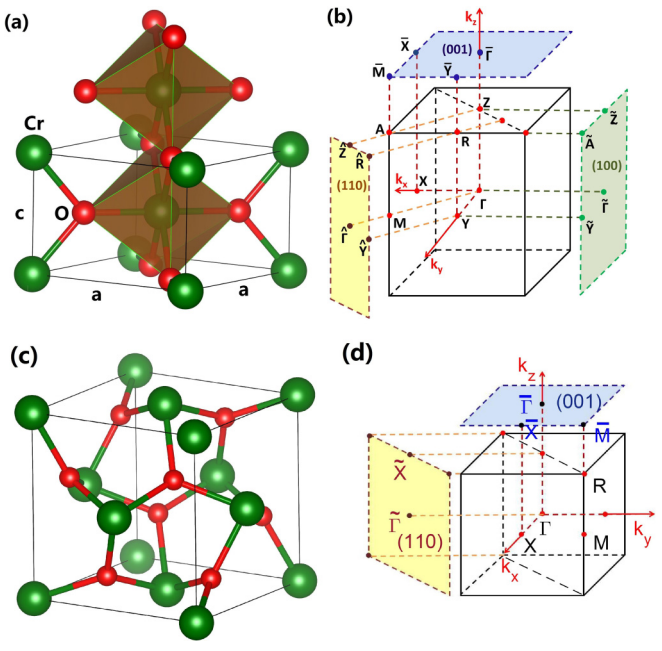

FIG. 1. Crystal structures and Brillouin zone (BZ). (a) r-CrO_2 with space group $P4_2/mnm$ (No. 136) and o-CrO_2 with space group $Pnnm$ (No. 58) with two nonequivalent lattice constants in the plane perpendicular to the c axis. (b) The bulk BZ and the corresponding surface BZ for r-CrO_2. (c) Crystal structure of p-CrO_2 with space group $Pa\bar{3}$ (No. 205). (d) The bulk BZ and the projected surface BZ for both (001) and (110) surfaces for p-CrO_2. Cr and O atoms are represented by green and red spheres, respectively.

The optimized lattice constants of r-CrO_2 are $a = 4.470$ Å and $c = 2.973$ Å, which nicely agree with the experimental values $a = 4.421$ Å and $c = 2.916$ Å [43]. Crystalline CrO_2 hosts a number of pressure-induced structural phases [44]. Under a pressure of 12–17 GPa [45], r-CrO_2 undergoes the structural transition to o-CrO_2 of the $CaCl_2$ type. o-CrO_2 with space group $Pnnm$ (No. 58), in which two lattice constants in the plane perpendicular to the c axis are nonequivalent, is very similar to r-CrO_2 [see Fig. 1(a)]. The calculated lattice constants are $a = 4.502$ Å, $b = 4.429$ Å, and $c = 2.968$ Å, which are in good agreement with the experimental values [45]. p-CrO_2 is demonstrated to be a stable FM half metal at a critical pressure of ~45 GPa [46], and it crystalizes in a simple-cubic lattice with symmorphic space group $Pa\bar{3}$ (No. 205), as shown Fig. 1(c). The optimized lattice constant is $a = 4.823$ Å, agreeing well with previous calculations [46]. All three phases of CrO_2 are confirmed to be half metals with a saturation magnetic moment of $2.00\mu_B$. It is worth noting that they share similar distorted CrO_6 octahedra, indicating that they host similar local chemical bonds.

III. RESULTS AND DISCUSSION

A. Electronic and topological features of r-CrO_2

In the absence of spin-orbital coupling (SOC), two spin channels of r-CrO_2 behave differently. Namely, the majority-spin states show metallic properties, while the minority-spin channel has an insulating band gap [see Fig. 2(a)]. Our calculations indicate that r-CrO_2 is completely spin polarized at the Fermi level and exhibits half-metallic properties, which is in excellent agreement with prior calculations [42,47] and experiments [48]. The symmorphic group elements of space group $P4_2/mnm$ contain inversion $\mathcal{I}$; twofold rotational symmetry C_2 axes oriented along [100], [010], and [110]; a fourfold rotational symmetry C_4 axis along [001] (i.e., the z axis); and mirror reflection M_z. In addition, the space group $P4_2/mnm$ also possesses nonsymmorphic symmetries such as $N_x = \{M_x|\tau\}$ and $N_{4z} = \{C_{4z}|\tau\}$, where $\tau = (\frac{1}{2}, \frac{1}{2}, \frac{1}{2})$ is the translation vector of one half of a body diagonal. The triple points (TPs) along the Γ-Z direction shown in Fig. 2(a) can be understood by considering symmorphic symmetries $\mathcal{I}$ and C_{4z} and the nonsymmorphic N_x. Based on symmetry transformation, we have the relation $N_x C_{4z} = C_{2z} T_{(0,-1,0)} (C_{4z} N_x)$ (where $T_{(0,-1,0)}$ is the translation operator acting on the Bloch wave function); that is, N_x and C_{4z} cannot commute (see the Supplemental Material (SM) [49]). Every momentum point along the Γ-Z direction is invariant under C_{4z} and N_x. Hence, the little group C_{4v} in the Γ-Z direction can require that a twofold-degenerate band always crosses two singly degenerate bands, resulting in the formation of two TPs, denoted as TP1 and TP2. These band crossings have been confirmed by recent angle-resolved photoelectron spectroscopy (ARPES) measurements [50]. In addition, two bands belonging to different C_2 eigenvalues $\pm i$ cross each other along the A-Z high-symmetry line. As a result, a type-II WP appears, which is protected by C_2 rotation symmetry along the [110] axis.

Due to weak SOC effects of both Cr and O elements, SOC has only an insignificant influence on electronic properties of CrO_2. Therefore, the half-metallic ferromagnetism is

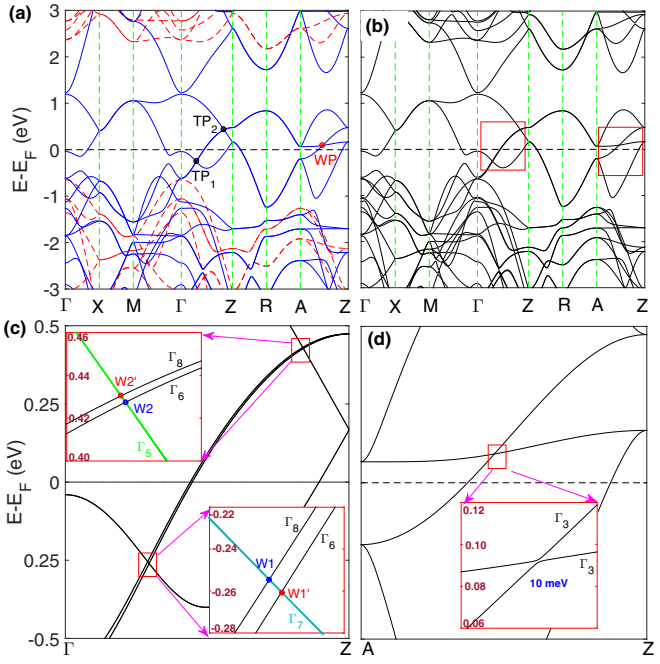

FIG. 2. Band structures of r-CrO_2. (a) Band structure without SOC. The majority- and minority-spin bands are denoted by the solid black and dashed red lines, respectively. Two TPs (i.e., TP1 and TP2) along the Γ-Z direction and a type-II WP along the A-Z direction are labeled. (b) Band structure in the presence of SOC with a [001] magnetization direction. (c) and (d) Enlarged views along the Γ-Z and A-Z directions in (b), respectively. $W1$ ($W1'$) and $W2$ ($W2'$) arise from TP1 and TP2 splitting, respectively, with [001] magnetization.

preserved in the presence of SOC, as shown in Fig. 2(b). Although r-CrO_2 exhibits similar band structures with and without SOC, they host different band topologies due to symmetry changes caused by the introduction of magnetization. It is worth mentioning that all possible magnetic configurations of r-CrO_2 are nearly degenerate, implying that magnetization directions can be easily manipulated by applying a magnetic field. As a result, r-CrO_2 hosts various Weyl fermions depending on the magnetization direction. Here, we pay attention only to the band topology of the [001] magnetization direction, and the analysis of the [100] magnetization direction is provided in the SM [49].

In the presence of SOC, two spin channels couple together, and the spin-rotation symmetry is broken. When the magnetization is along the [001] direction, the symmetry of r-CrO_2 is reduced to the magnetic point group $D_{4h}(C_{4h})$. In this case, C_2 rotational symmetries along the [100], [010], and [110] axes are broken, while the magnetic symmetry $\mathcal{T}C_2$ is still maintained. The little group of $\mathbf{k}(0,0,k_z)$ along Γ-Z is C_4, and the mirror reflection along this direction is broken. As shown in Fig. 2(c), the intrinsic magnetization along the [001] direction will split the doubly degenerate band into two singly degenerate bands denoted by Γ_6 ($e^{-i\frac{\pi}{4}}$) and Γ_8 ($e^{i\frac{3\pi}{4}}$), which cross bands Γ_5 ($e^{-i\frac{\pi}{4}}$) and Γ_7 ($e^{i\frac{5\pi}{4}}$), respectively, where Γ_5, Γ_6, Γ_7, and Γ_8 are the irreducible representations of fourfold rotation C_{4z}. Therefore, each TP splits into two type-I WPs with opposite chirality; that is, TP1 is degenerated to WPs $W1$ and $W1'$, and TP2 is degenerated to WPs $W2$ and $W2'$.

TABLE I. Nodal-points of r-CrO_2 without and with SOC along the [001] magnetization direction. The WP in the absence of SOC is type-II. The coordinates in momentum space, Chern numbers, and the energies relative to E_F are listed, respectively. The coordinates of other WPs are related to the ones listed by the symmetries, $\mathcal{P}$, C_{4z}, $\mathcal{T}C_{2x}$, and $\mathcal{T}C_{2y}$.

	Nodal point	Coordinates $[k_x(2\pi/a), k_y(2\pi/a), k_z(2\pi/c)]$	Chern number	$E-E_F$ (eV)
Without SOC	TP1	(0, 0, 0.1461)		−0.256
	TP2	(0, 0, 0.4188)		0.428
	WP	(0.2669 0.2669 0.5)	+1	0.092
With SOC	$W1$	(0, 0, 0.1451)	−1	−0.254
	$W1'$	(0, 0, 0.1477)	+1	−0.260
	$W2$	(0, 0, 0.4193)	−1	0.427
	$W2'$	(0, 0, 0.4181)	+1	0.430
	$W3$	(0.1897, 0, 0.1069)	+1	−0.279
	$W4$	(0.1056, 0.1038, 0.0941)	−1	−0.223

The [001] magnetization destroys the type-II WP along A-Z with a nontrivial gap opening of ∼10 meV [see Fig. 2(d)], as the symmetry $\mathcal{T}C2_{110}$ does not allow band crossings on this line. Interestingly, this type-II WP may survive with the magnetization along the [100] direction, resulting in the coexistence of type-I and type-II WPs in r-CrO_2 [49]. In contrast, the existence of WPs in high-symmetry k_x-k_z and k_y-k_z planes is allowed by the antiunitary symmetries $\mathcal{T}C_{2y}$ and $\mathcal{T}C_{2x}$, respectively (see the SM [49]). Through careful analysis, we find that WPs $W3$, which relate to $\mathcal{I}$, $\mathcal{T}C_{2x}$, and $\mathcal{T}C_{2y}$, are present in the k_x-k_z and k_y-k_z planes. In addition, we also find that WPs $W4$ locate near the $k_x = k_y$ and $k_x = -k_y$ planes, and these WPs related by $\mathcal{I}$ and C_{4z} are accidental nodal points, which do not correspond to any little-group symmetry. Hence, WPs $W4$ are not stable and easily annihilate each other. The precise coordinates, Chern numbers, and energies related to the Fermi level E_F of the nodal points are listed in Table I. The Chern numbers are calculated using the Z2PACK package [51], in which the Wilson-loop method on a sphere around WPs is employed [52,53].

B. Electronic and topological features of o-CrO_2

In comparison with r-CrO_2, o-CrO_2 (space group $Pnnm$) hosts a similar lattice structure and local chemical bonds, so it exhibits half-metallic features and hosts similar band structures. However, the detailed topological features of o-CrO_2 are essentially different from those of r-CrO_2 due to the lower symmetry of o-CrO_2. In the absence of SOC, o-CrO_2 possesses the point group D_{2h}. The little group along Γ-Z is C_{2v}, which cannot protect the TPs along this line but can allow the existence of WPs (see Fig. S3 in the SM [49]). In addition, in comparison with r-CrO_2, o-CrO_2 does not possess WPs along Z-A due to the absence of twofold rotational symmetry C_2 along this line.

In the presence of SOC, we discuss only the case of [001] magnetization. The corresponding band structure is shown in Fig. 3. With a magnetization along the [001] direction, the symmetry of o-CrO_2 reduces to the magnetic point group $D_{2h}(C_{2h})$. The four WPs along Γ-Z survive, protected by C_{2z}. Namely,

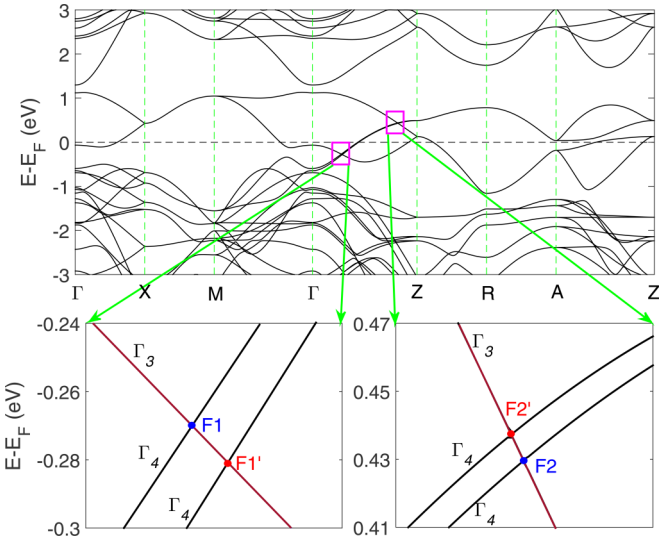

FIG. 3. The electronic band structures of o-CrO_2 in the presence of SOC with magnetization along the [001] direction. The bottom panels show enlarged views of two crossing regions along Γ-Z. The WPs $F1$ ($F1'$) and $F2$ ($F2'$) are denoted by solid circles, which are marked by red and blue, representing the WPs with Chern numbers $+1$ and -1, respectively.

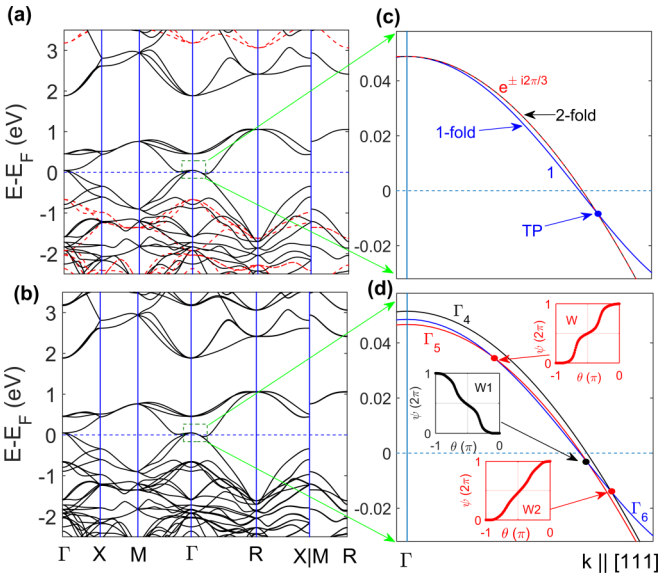

FIG. 4. The band structures of p-CrO_2. (a) Band structure without SOC. The majority- and minority-spin bands are denoted by the solid black and dashed red lines, respectively. (b) The SOC band structure with the magnetization along the [111] direction. (c) and (d) Enlarged views along the Γ-R direction (or $\mathbf{k} \parallel [111]$) near the Γ point in (a) and (b), respectively. The insets in (d) show the Chern numbers of WPs determined by the Wilson-loop method.

the crossing bands belong to irreducible representations Γ_3 and Γ_4 of C_{2z}. In addition, the antiunitary symmetries $\mathcal{T}C_{2x}$ and $\mathcal{T}C_{2y}$ allow the existence of WPs in high-symmetry planes k_x-k_z and k_y-k_z, and the related WPs $F3$ and $F4$ are found. We also find another kind of WP, $F5$, related by $\mathcal{P}$ and C_{2z}. WPs $F5$ are generic nodal points and are not stable in principle. We list the WPs of o-CrO_2 with [001] magnetization in Table II.

C. Electronic and topological features of p-CrO_2

The band structures of p-CrO_2 without and with SOC are illustrated in Figs. 4(a) and 4(b), respectively, indicating the half-metallic features of p-CrO_2. In the absence of SOC, the symmetry group contains four threefold rotational symmetry C_3 axes (i.e., [111], [1$\bar{1}$1], [11$\bar{1}$], and [$\bar{1}$11]) plus inversion I and three mirror symmetries M_i ($i = x,y,z$). From the magnified view of the band structure along Γ-R (or $\mathbf{k} \parallel [111]$) in Fig. 4(c), we can see that a nodal point locates $\sim$10 meV below the Fermi level. This crossing point is a TP. Different from those protected by C_{4v} in r-CrO_2, the TP on Γ-R in p-CrO_2 is protected by the threefold rotational symmetry along the [111] axis C_3^{111} [8,9,54].

In the presence of SOC, the [111] easy axis is found to be the energetically most favorable magnetization direction. The presence of SOC with a magnetization along the [111] direction breaks the mirror reflection symmetries M_i ($i = x,y,z$). The corresponding magnetic space group with the [111] magnetization direction contains only six elements formed by two

TABLE II. WPs of o-CrO_2 in the presence of SOC with the magnetization along the [001] direction. The positions in momentum space, Chern numbers, and energies relative to E_F are listed. The coordinates of the other WPs are related to the ones listed by symmetries, $\mathcal{P}$, $\mathcal{T}C_{2y}$, $\mathcal{T}C_{2x}$, and C_{2z}.

Nodal point	Coordinates [$k_x(2\pi/a)$, $k_y(2\pi/b)$, $k_z(2\pi/c)$]	Chern number	$E - E_F$ (eV)
$F1$	(0, 0, 0.1378)	-1	-0.270
$F1'$	(0, 0, 0.1397)	$+1$	-0.281
$F2$	(0, 0, 0.4089)	-1	0.430
$F2'$	(0, 0, 0.4078)	-1	0.435
$F3$	(0.1891, 0, 0.1013)	$+1$	-0.306
$F4$	(0, 0.1443 0.1224)	$+1$	-0.279
$F5$	(0.1643, 0.0429, 0.0991)	-1	-0.282

TABLE III. WPs of p-CrO_2 in the presence of SOC along the [111] magnetization direction. It must be noted that the TP occurs in the absence of SOC. The positions, Chern numbers, and energies relative to E_F are listed. $W1$ and $W2$ with opposite Chern numbers are the type-II WPs formed by the splitting of the TP in the presence of SOC. WP $W2$ is the crossing between the Nth and $(N+1)$th bands, while the others are the crossings between the $(N-1)$th and Nth bands. The coordinates of the other WPs are related to the ones listed by the inversion symmetry $\mathcal{I}$.

Nodal point	Coordinates [$k_x(2\pi/a)$, $k_y(2\pi/a)$, $k_z(2\pi/a)$]	Chern number	$E - E_F$ (meV)
TP	(0.0641, 0.0641, 0.0641)		-10
W	(0.0269, 0.0269, 0.0269)	$+1$	$+36$
$W1$	(0.0621, 0.0621, 0.0621)	-1	-6
$W2$	(0.0687, 0.0687, 0.0687)	$+1$	-15
$W3$	(0.0011, 0.1414, 0.0842)	$+1$	111
$W4$	(0.0907, 0.0006, 0.1613)	$+1$	137
$W5$	(0.1419, 0.0844, 0.0010)	$+1$	141

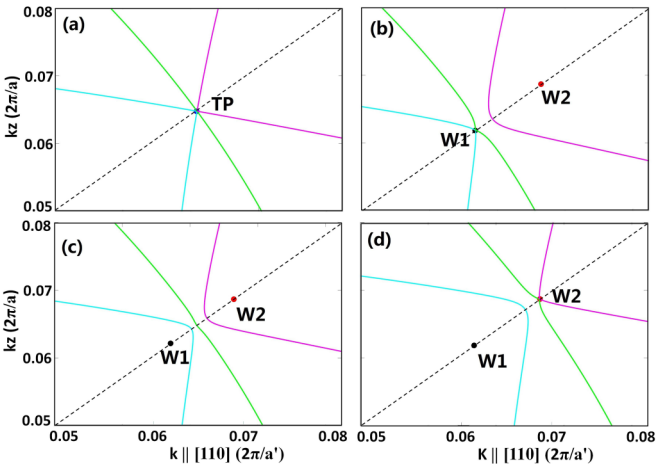

FIG. 5. Fermi surface at the $k_x = k_y$ [or (110)] plane. A part of the BZ is shown, and $a' = \frac{\sqrt{2}}{2}a$. (a) Without SOC, E_F is set to the TP ($E_F = -10$ meV), and contact between electron and hole pockets occurs at this point. With SOC, E_F is gradually tuned from $W1$ to $W2$, the electron and hole pockets (b) occur at $W1$ ($E_F = -6$ meV), (c) disconnect ($E_F = -10$ meV), and (d) occur at $W2$ ($E_F = -15$ meV). The contour lines formed by bands $N-1$, N, and $N+1$ are shown in cyan, green, and magenta, respectively.

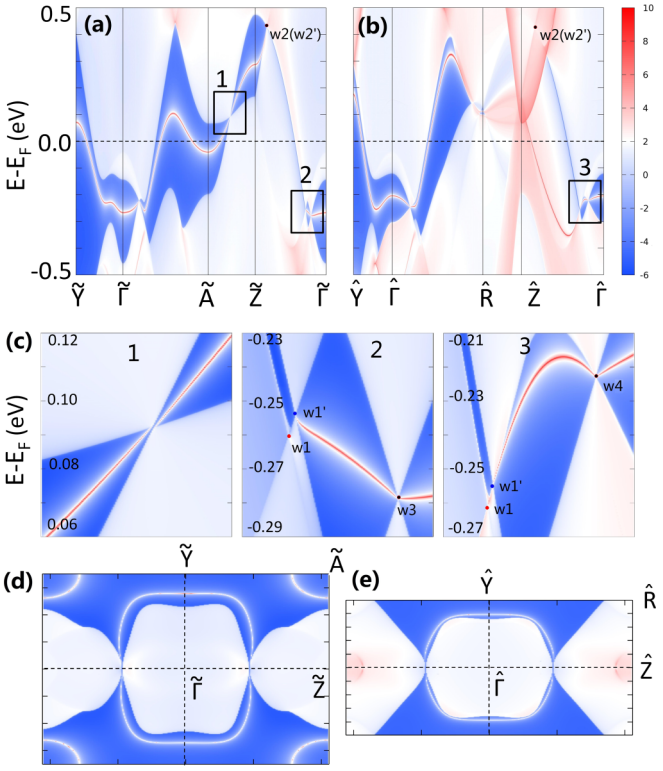

FIG. 6. Surface states and Fermi arcs of r-CrO_2. The energy bands projected on the (a) (100) and (b) (110) surfaces. (c) The regions denoted by 1, 2, and 3 in (a) and (b) are enlarged in the left, middle, and right panels, respectively. The red and blue dots indicate the projections of WPs with Chern numbers $+1$ and -1, respectively. The black dots are projected from two WPs with opposite chirality. The Fermi arcs projected on the (d) (100) and (e) (110) surfaces.

generators: inversion $\mathcal{I}$ and C_3 symmetry along the [111] axis. With magnetization along this axis, the eigenvalues can be distinguished by the irreducible representations of threefold symmetry C_3 as $e^{i\frac{\pi}{3}}$ for Γ_4, $e^{-i\frac{\pi}{3}}$ for Γ_5, and $e^{-i\pi}$ for Γ_6. The effective Zeeman field of SOC leads to the twofold-degenerate band splitting into two singly degenerate bands, and each band corresponds to either of the two irreducible representations, Γ_4 and Γ_5. As shown in Fig. 4, the band Γ_6 will respectively cross the Γ_4 and Γ_5 bands, forming two WPs with opposite Chern numbers, denoted as $W1$ and $W2$. Another WP, W, induced by the band crossing between Γ_5 and Γ_6 is also present. Their precise positions in momentum space, Chern numbers, and energies related to the Fermi level E_F are listed in Table III.

The nontrivial properties in topological metals do not simply depend on the relations between valence and conduction bands because the occupied states are functions of the crystal momentum $\mathbf{k}$ [23]. For instance, the WP $W2$ is the crossing point between the Nth and $(N+1)$th bands, where N is the total number of valence electrons in a primitive cell of p-CrO_2. The WPs W and $W1$ are formed by the crossings of valence bands $N-1$ and N. In addition, we find more WPs between the bands $N-1$ and N, some of which are close to E_F, denoted as $W3$, $W4$, and $W5$. In comparison with the WPs on Γ-R, these WPs are accidental nodal points without the protection of any little group and are not stable with respect to perturbation. Detailed information about these WPs is also listed in Table III. Importantly, there is only one pair of symmetry-protected WPs $W2$ forming at the boundary of electron and hole pockets, while the other WPs arise at the crossing points of two pockets of the same carriers. Therefore, the surface Fermi arcs from the projections of two type-II WPs $W2$ may be clear and will be easy to observe in experiments.

The TP without SOC and WPs with SOC in p-CrO_2 located on the Γ-R axis are type II [6,7]. This can be verified by examining the Fermi surface at the $k_x = k_y$ [or (110)] plane. Without SOC, the hole and electron pockets touch at the position of the TP [Fig. 5(a)]. With SOC, when E_F is tuned to $W1$, the hole and electron pockets touch at the position of $W1$ between bands $N-1$ and N, as shown in Fig. 5(b). A further decrease of E_F separates the electron and hole pockets [Fig. 5(c)], and the pockets will touch again when E_F is tuned to the energy of $W2$.

D. Surface states and Fermi arcs

Based on the maximally localized Wannier functions [55,56], we obtain the surface states using the iterative Green's function method [57] as implemented in the WANNIERTOOLS package [58]. We calculate the surface states of r-CrO_2 projected on (001), (100), and (110) surfaces, respectively. We find that the topologically protected surface states projected onto (100) and (110) surfaces are clearly visible in Figs. 6(a) and 6(b), respectively. The surface states on the (001) surface are mostly hidden in the projection of bulk states, which are supplied in the SM [49]. The band gap arising from the type-II WP with SOC is nontrivial, exhibiting visible surface states along $\tilde{A}$-$\tilde{Z}$ [see the left panel of Fig. 6(c)]. The WPs $W1$ ($W1'$) and $W2$ ($W2'$) projected onto the (100) and (110) surfaces are different. However, only $W1'$ is apparent, and its projection acts as the termination of surface Fermi arcs, while

the projections of other WPs are hidden in bulk states, as shown in Figs. 6(a)–6(c). The WP $W3$ projected on the (100) surface locates on $\tilde{\Gamma}$-$\tilde{Z}$ [see the middle panel of Fig. 6(c)]. There are two topological surface states terminated at the projection of $W3$ since this surface Dirac point projected from two WPs with opposite chirality. Similarly, the projection of $W4$ on the (110) surface also exhibits two nontrivial surface states which are distributed on two sides of the surface Dirac core, shown in the right panel of Fig. 6(c). The projections of the bulk Fermi surface onto the (100) and (110) surfaces are shown in Figs. 6(d) and 6(e), respectively. The nontrivial Fermi arcs are clearly visible and very long, making them easy to observe in ARPES. The compounds o-CrO_2 and p-CrO_2 also exhibit visible Fermi arcs and are included in the SM [49].

E. Quasiparticle interference

The surface Fermi arcs are crucial properties associated with the topological nontrivial features of bulk WPs. On the one hand, the surface Fermi arcs can be directly confirmed by ARPES. On the other hand, they will exhibit unique signatures in quasiparticle interference (QPI) and can be observed via spectroscopy measurements using scanning tunneling microscopy. Compared with the projected Fermi surface of nonmagnetic WSMs in which Fermi arcs are spin textured and time-reversal symmetry prevents scattering between the states with opposite spins, the spin-polarized Fermi arcs in half-metallic CrO_2 will exhibit single-spin scattering. Hence, the QPI pattern of surface states is mainly dominated by initial and final states in momentum space. It can be approximated by the joint density of states (JDOS) as a function of momentum difference $\mathbf{q}$ [59]:

$$J(\mathbf{q},\epsilon) = \int d^2\mathbf{k}_\parallel \rho^0(\mathbf{k}_\parallel,\epsilon)\rho^0(\mathbf{k}_\parallel+\mathbf{q},\epsilon), \qquad (1)$$

where $\rho^0(\mathbf{k}_\parallel,\epsilon) = -\frac{1}{\pi}\mathrm{Im}[\mathrm{Tr}\mathbf{G}(\mathbf{k}_\parallel,\epsilon)]$ is the momentum-resolved surface density of states of a clean sample and $\mathbf{G}(\mathbf{k}_\parallel,\epsilon)]$ is the surface Green's function at surface momentum vector $\mathbf{k}_\parallel$ and energy ϵ relative to the Fermi level. The weighted Fermi arcs of r-CrO_2 with only the surface contribution on the (100) and (110) surfaces are shown in Figs. 7(a) and 7(b). We can see that the open Fermi arcs have a nearly constant spectral density. Based on the curvature of the weighted Fermi arcs, we can identify four different groups of scattering wave vectors for two surfaces, i.e., Q_1 to Q_4 for the (100) surface and q_1 to q_4 for the (110) surface. Figures 7(c) and 7(d) illustrate the JDOS patterns for (100) and (110) surfaces of r-CrO_2, respectively. In addition, the QPI pattern of p-CrO_2 is clearly visible (see Fig. S4 in the SM [49]).

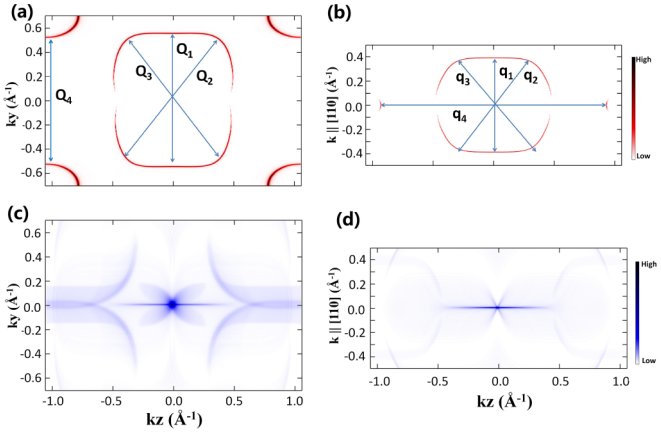

FIG. 7. The weighted Fermi arcs and JDOS of r-CrO_2. The weighted Fermi arcs with only a surface contribution on (a) the (100) and (b) (110) surfaces. The scattering wave vectors are denoted by Q_1 (q_1) to Q_4 (q_4) for the (100) [(110)] surface. The JDOS patterns for (c) the (100) and (d) (110) surfaces related to the scattering wave vectors are visible.

IV. SUMMARY

In summary, we proposed that FM Weyl fermions can exist in three different phases of CrO_2. The breaking of spin-rotation symmetry leads to the tunability of Weyl fermions, which can be easily realized by manipulating the magnetization direction. In particular, r-CrO_2 is an ideal candidate to investigate FM topological semimetals, possessing potential topology-related applications at room temperature. In addition, the topological features in different phases of CrO_2 may establish the strong relationship between the band topology and local chemical bonding. The topologically protected surface states and Fermi arcs are clearly visible. Our findings strongly suggest that CrO_2 not only provides a promising platform to investigate the symmetry-protected topological order but also provides an exotic avenue to search for the desired FM topological semimetals in a framework of band structures arising from local atomic orbitals.

ACKNOWLEDGMENTS

This work is supported by the National Natural Science Foundation of China (NSFC Grants No. 11674148, No. 11334004, and No. 91634106) and the Guangdong Natural Science Funds for Distinguished Young Scholars (Grant No. 2017B030306008).

R.W. and Y.J.J. contributed equally to this work.

[1] Z. Wang, Y. Sun, X.-Q. Chen, C. Franchini, G. Xu, H. Weng, X. Dai, and Z. Fang, Phys. Rev. B **85**, 195320 (2012).

[2] Z. K. Liu, B. Zhou, Y. Zhang, Z. J. Wang, H. M. Weng, D. Prabhakaran, S.-K. Mo, Z. X. Shen, Z. Fang, X. Dai *et al.*, Science **343**, 864 (2014).

[3] X. Wan, A. M. Turner, A. Vishwanath, and S. Y. Savrasov, Phys. Rev. B **83**, 205101 (2011).

[4] A. A. Burkov and L. Balents, Phys. Rev. Lett. **107**, 127205 (2011).

[5] G. Xu, H. Weng, Z. Wang, X. Dai, and Z. Fang, Phys. Rev. Lett. **107**, 186806 (2011).

[6] Y. Xu, F. Zhang, and C. Zhang, Phys. Rev. Lett. **115**, 265304 (2015).

[7] A. A. Soluyanov, D. Gresch, Z. Wang, Q. Wu, and M. Troyer, Nature (London) **527**, 495 (2015).

[8] B. Q. Lv, Z.-L. Feng, Q.-N. Xu, X. Gao, J.-Z. Ma, L.-Y. Kong, P. Richard, Y.-B. Huang, V. N. Strocov, C. Fang *et al.*, Nature (London) **546**, 627 (2017).

[9] Z. Zhu, G. W. Winkler, Q. S. Wu, J. Li, and A. A. Soluyanov, Phys. Rev. X **6**, 031003 (2016).

[10] A. A. Burkov, M. D. Hook, and L. Balents, Phys. Rev. B **84**, 235126 (2011).

[11] B. J. Wieder, Y. Kim, A. M. Rappe, and C. L. Kane, Phys. Rev. Lett. **116**, 186402 (2016).

[12] H. Weng, C. Fang, Z. Fang, B. A. Bernevig, and X. Dai, Phys. Rev. X **5**, 011029 (2015).

[13] C. Fang, Y. Chen, H.-Y. Kee, and L. Fu, Phys. Rev. B **92**, 081201 (2015).

[14] Y. X. Zhao, A. P. Schnyder, and Z. D. Wang, Phys. Rev. Lett. **116**, 156402 (2016).

[15] C.-K. Chiu and A. P. Schnyder, Phys. Rev. B **90**, 205136 (2014).

[16] J. Zak, Phys. Rev. Lett. **62**, 2747 (1989).

[17] J. Liu and D. Vanderbilt, Phys. Rev. B **90**, 155316 (2014).

[18] A. A. Burkov, Phys. Rev. Lett. **113**, 187202 (2014).

[19] S.-M. Huang, S.-Y. Xu, I. Belopolski, C.-C. Lee, G. Chang, B. Wang, N. Alidoust, G. Bian, M. Neupane, C. Zhang *et al.*, Nat. Commun. **6**, 7373 (2015).

[20] J. Ruan, S.-K. Jian, H. Yao, H. Zhang, S.-C. Zhang, and D. Xing, Nat. Commun. **7**, 11136 (2016).

[21] J. Ruan, S.-K. Jian, D. Zhang, H. Yao, H. Zhang, S.-C. Zhang, and D. Xing, Phys. Rev. Lett. **116**, 226801 (2016).

[22] G. Autès, D. Gresch, M. Troyer, A. A. Soluyanov, and O. V. Yazyev, Phys. Rev. Lett. **117**, 066402 (2016).

[23] Z. Wang, D. Gresch, A. A. Soluyanov, W. Xie, S. Kushwaha, X. Dai, M. Troyer, R. J. Cava, and B. A. Bernevig, Phys. Rev. Lett. **117**, 056805 (2016).

[24] Z. Wang, M. G. Vergniory, S. Kushwaha, M. Hirschberger, E. V. Chulkov, A. Ernst, N. P. Ong, R. J. Cava, and B. A. Bernevig, Phys. Rev. Lett. **117**, 236401 (2016).

[25] Y. Xu, C. Yue, H. Weng, and X. Dai, Phys. Rev. X **7**, 011027 (2017).

[26] R. Wang, J. Z. Zhao, Y. J. Jin, W. P. Xu, L.-Y. Gan, X. Z. Wu, H. Xu, and S. Y. Tong, Phys. Rev. B **96**, 121104(R) (2017).

[27] Y. J. Jin, R. Wang, Z. J. Chen, J. Z. Zhao, Y. J. Zhao, and H. Xu, Phys. Rev. B **96**, 201102(R) (2017).

[28] S.-Y. Xu, I. Belopolski, N. Alidoust, M. Neupane, G. Bian, C. Zhang, R. Sankar, G. Chang, Z. Yuan, C.-C. Lee *et al.*, Science **349**, 613 (2015).

[29] A. Tamai, Q. S. Wu, I. Cucchi, F. Y. Bruno, S. Riccò, T. K. Kim, M. Hoesch, C. Barreteau, E. Giannini, C. Besnard *et al.*, Phys. Rev. X **6**, 031021 (2016).

[30] G. Chang, S.-Y. Xu, X. Zhou, S.-M. Huang, B. Singh, B. Wang, I. Belopolski, J. Yin, S. Zhang, A. Bansil *et al.*, Phys. Rev. Lett. **119**, 156401 (2017).

[31] S. Jia, S.-Y. Xu, and M. Z. Hasan, Nat. Mater. **15**, 1140 (2016).

[32] R. A. de Groot, F. M. Mueller, P. G. van Engen, and K. H. J. Buschow, Phys. Rev. Lett. **50**, 2024 (1983).

[33] L. Chioncel, H. Allmaier, E. Arrigoni, A. Yamasaki, M. Daghofer, M. I. Katsnelson, and A. I. Lichtenstein, Phys. Rev. B **75**, 140406 (2007).

[34] B. Bradlyn, L. Elcoro, J. Cano, M. G. Vergniory, Z. Wang, C. Felser, M. I. Aroyo, and B. A. Bernevig, Nature (London) **547**, 298 (2017).

[35] G. Kresse and J. Furthmüller, Phys. Rev. B **54**, 11169 (1996).

[36] G. Kresse and J. Furthmüller, Comput. Mater. Sci. **6**, 15 (1996).

[37] W. Kohn and L. J. Sham, Phys. Rev. **140**, A1133 (1965).

[38] P. E. Blöchl, Phys. Rev. B **50**, 17953 (1994).

[39] J. P. Perdew, K. Burke, and M. Ernzerhof, Phys. Rev. Lett. **77**, 3865 (1996).

[40] J. P. Perdew, K. Burke, and M. Ernzerhof, Phys. Rev. Lett. **78**, 1396 (1997).

[41] A. I. Liechtenstein, V. I. Anisimov, and J. Zaanen, Phys. Rev. B **52**, R5467(R) (1995).

[42] M. A. Korotin, V. I. Anisimov, D. I. Khomskii, and G. A. Sawatzky, Phys. Rev. Lett. **80**, 4305 (1998).

[43] M. S. Anwar and J. Aarts, Phys. Rev. B **88**, 085123 (2013).

[44] S. Kim, K. Kim, C.-J. Kang, and B. I. Min, Phys. Rev. B **85**, 094106 (2012).

[45] B. R. Maddox, C. S. Yoo, D. Kasinathan, W. E. Pickett, and R. T. Scalettar, Phys. Rev. B **73**, 144111 (2006).

[46] Y. Li and J. Hao, Solid State Commun. **152**, 1216 (2012).

[47] K. Schwarz, J. Phys. F **16**, L211 (1986).

[48] Y. Ji, G. J. Strijkers, F. Y. Yang, C. L. Chien, J. M. Byers, A. Anguelouch, G. Xiao, and A. Gupta, Phys. Rev. Lett. **86**, 5585 (2001).

[49] See Supplemental Material at http://link.aps.org/supplemental/10.1103/PhysRevB.97.195157 for the topological properties of the [100] magnetization for r-CrO_2, the [001] magnetization for p-CrO_2, and the symmetry analysis and low-energy kp Hamiltonian on the band topology, which includes Refs. [8,9,23,45,54,59,60].

[50] F. Bisti, V. A. Rogalev, M. Karolak, S. Paul, A. Gupta, T. Schmitt, G. Güntherodt, V. Eyert, G. Sangiovanni, G. Profeta *et al.*, Phys. Rev. X **7**, 041067 (2017).

[51] D. Gresch, G. Autès, O. V. Yazyev, M. Troyer, D. Vanderbilt, B. A. Bernevig, and A. A. Soluyanov, Phys. Rev. B **95**, 075146 (2017).

[52] R. Yu, X. L. Qi, A. Bernevig, Z. Fang, and X. Dai, Phys. Rev. B **84**, 075119 (2011).

[53] A. A. Soluyanov and D. Vanderbilt, Phys. Rev. B **83**, 035108 (2011).

[54] G. Chang, S.-Y. Xu, S.-M. Huang, D. S. Sanchez, C.-H. Hsu, G. Bian, Z.-M. Yu, I. Belopolski, N. Alidoust, H. Zheng *et al.*, Sci. Rep. **7**, 1688 (2017).

[55] N. Marzari, A. A. Mostofi, J. R. Yates, I. Souza, and D. Vanderbilt, Rev. Mod. Phys. **84**, 1419 (2012).

[56] A. A. Mostofi, J. R. Yates, Y. S. Lee, I. Souza, D. Vanderbilt, and N. Marzari, Comput. Phys. Commun. **178**, 685 (2008).

[57] M. P. L. Sancho, J. M. L. Sancho, and J. Rubio, J. Phys. F **14**, 1205 (1984).

[58] Q. Wu, S. Zhang, H.-F. Song, M. Troyer, and A. A. Soluyanov, Comput. Phys. Commun. **224**, 405 (2018).

[59] S. Kourtis, J. Li, Z. Wang, A. Yazdani, and B. A. Bernevig, Phys. Rev. B **93**, 041109 (2016).

[60] T. L. Hughes, E. Prodan, and B. A. Bernevig, Phys. Rev. B **83**, 245132 (2011).